Gap-surface plasmon metasurfaces for broadband circular-to-linear polarization conversion and vector vortex beam generation

Heiden, Jacob. T.; Ding, Fei; Linnet, Jes; Yang, Yuanqing; Beermann, Jonas; Bozhevolnyi, Sergey I.

Go to publication entry in University of Southern Denmark's Research Portal

WILEY-VCH

Gap-surface Plasmon Metasurfaces for Broadband Circular-to-linear Polarization Conversion and Vector Vortex Beam Generation

Jacob T. Heiden, Fei Ding*, Jes Linnet, Yuanqing Yang*, Jonas Beermann, and Sergey I. Bozhevolnyi

((Optional Dedication))

Jacob T. Heiden, Dr. Fei Ding, Jes Linnet, Dr. Yuanqing Yang, Prof. Jonas Beermann, and Prof. Sergey I. Bozhevolnyi
Centre for Nano Optics, University of Southern Denmark, Campusvej 55, DK-5230 Odense, Denmark
E-mail: feid@mci.sdu.dk and yy@mci.sdu.dk

Abstract: The ability to control and manipulate the polarization state of light is of crucial importance in many modern optical applications ranging from quantum technologies to biomedical sciences. Here we design, fabricate, and experimentally demonstrate an ultrathin quarter-wave plate (QWP) with a gap-surface plasmon metasurface, allowing for broadband and efficient conversion between circular and linear polarizations with ~85% average reflectance across a 200-nm-wide bandwidth in the near-infrared range (750–950 nm). Based on the QWP design, we further derive a general method to generate vector vortex beams (VVBs) that possess spatially-varied distributions of the polarization vector and carry specified orbital angular momentums (OAMs) by using space-variant QWP unit cells. The fabricated metasurface exhibits highly-efficient VVB generation over a wavelength range from 750 to 950 nm, with the average efficiencies of ~72% and ~68% for the right circularly-polarized (RCP) and left circularly-polarized (LCP) incident light, respectively. The developed approach allows one to realize compact, cost-effective and high-performance polarization converters, paving the way for ultimate miniaturization of optical devices with arbitrary control of light fields.

1

1. Introduction

One of the most important functionalities realized in modern optical instrumentations is the ability to fully control the polarization state of light, which is an intrinsic and import characteristic of electromagnetic radiation. Conventional optical components enabling polarization manipulation typically rely on birefringent materials, such as quartz or mica, which provide the phase retardation between two orthogonally polarized components during light propagation.[1] Consequently, the resulting devices are inherently bulky and voluminous, thereby severely limiting the possibilities of miniaturizing and densely-integrating photonic systems to the nanoscale.

Metasurfaces, the two-dimensional analogs of metamaterials composed of ultrathin arrays of planar nanostructures that provide unprecedented control over the transmitted and reflected optical fields, have attracted increasing attention due to their great potentials for ultra-thin, high-performance, and cost-effective optical devices.[2-4] By tailoring the optical responses of properly designed and arranged resonant subwavelength elements, the phase, amplitude, and polarization of optical fields can be controlled at will, thereby resulting in numerous applications and compact devices, including beam deflectors,[5-10] flat lenses,[11-17] holograms,[18-22] surface wave couplers,[23-27] and polarimeters.[28-31] Especially, highly-efficient wave plates have been successfully demonstrated by using gap-surface plasmon (GSP) metasurfaces, which function as effective wave retarders to manipulate the polarization state of light in the reflection mode at the nanoscale.[32-40] For instance, half-wave plates (HWPs) that enable orthogonal linear-polarization conversion have been realized in the near-infrared,[32,34-35] middle-infrared[36] and terahertz range.[37] In spite of the successful demonstration of HWPs, the realization of quarter-wave plates (QWPs) was rarely addressed experimentally, especially at optical frequencies. At the same time, it is highly desirable to replace the conventional bulky QWPs with metasurface-based ultrathin QWPs that are

capable of interconverting circularly-polarized (CP) and linearly-polarized (LP) waves in a broad spectrum range.

In this paper, we utilize GSP metasurfaces to design and experimentally demonstrate an ultrathin QWP, which allows for broadband and efficient conversion between circular and linear polarizations with ~85% average reflectance across a 200-nm-wide bandwidth in the near-infrared range (750–950 nm). Furthermore, we derive a general method to generate vector vortex beams (VVBs) that possess spatially-varied distributions of the polarization vector and carry specified orbital angular momentums (OAMs) by using space-variant QWP unit cells, mimicking the typical bulky VVB generators,[41,42] which may find potential applications in photonics and quantum science.[43-47] The suggested approach allows one to combine the functionalities of typical vector beams and vortex beams, with superior characteristics to reported metasurfaces-based vector beam generators with narrower operating bandwidth,[14,48,49] vortex beam generators with considerably low efficiencies,[50-54] and VVB generators using cascaded structures[55] or complicated design.[56] The fabricated metasurface enables efficient generation of radially-polarized (RP) and azimuthally-polarized (AP) beams while carrying OAMs of $l = -1$ and $l = +1$, over a wavelength range from 750 to 950 nm, with the averaging efficiencies of ~72% and ~68% for the right circularly-polarized (RCP) and left circularly-polarized (LCP) incident light, respectively.

2. Design of the Broadband QWP for LP Light Generation and Manipulation

2.1. Design of the Broadband QWP

Figure 1a schematically illustrates the configuration of a basic metal-insulator-metal (MIM) unit cell that comprises the QWP, which consists of a gold (Au) nanobrick, a subwavelength silicon dioxide (SiO_2) spacer layer and a continuous Au film, forming a typical GSP resonator.[39,40] The MIM unit cells are periodically distributed in both the x- and y-directions with a subwavelength periodicity of $\Lambda = 240$ nm, which can eliminate unwanted diffraction orders and propagating surface plasmon polaritons. The thickness of middle SiO_2 space layer

WILEY-VCH

is optimized to be $w = 50$ nm, ensuring good performance and sufficient phase response at the

design wavelength of $\lambda = 850$ nm. The thickness of Au nanobricks is $t = 50$ nm and the

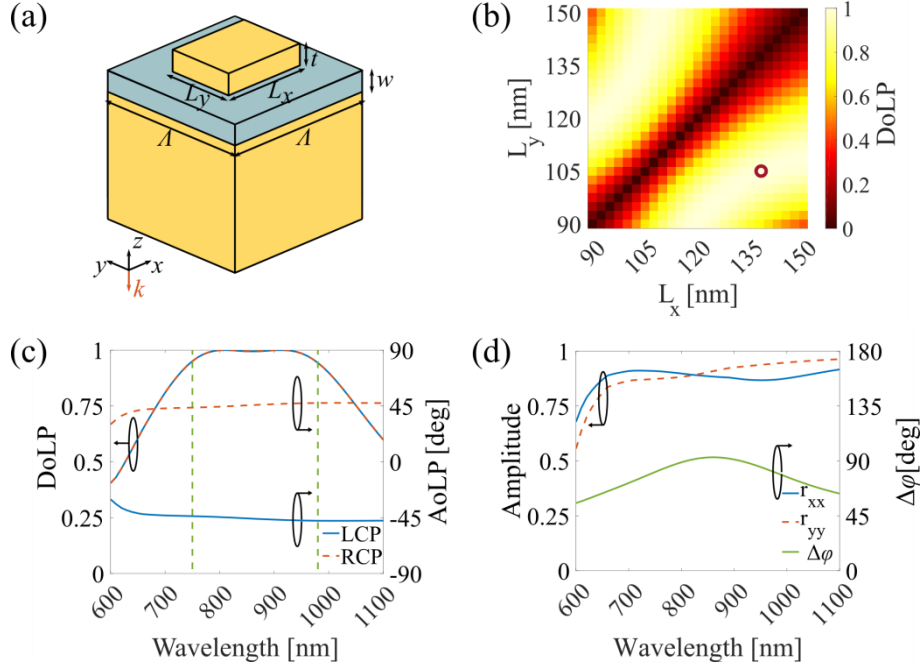bottom Au layer is thick enough to block light transmission.

Figure 1 (a) Schematic of an Au-SiO$_2$-Au MIM unit cell. (b) Simulated degree of linear

polarization (DoLP) as a function of the nanobrick dimensions (L_x and L_y) at the design

wavelength of $\lambda = 850$ nm. The optimized dimensions ($L_x = 138$ nm and $L_y = 105$ nm) are

indicated with a circle. (c) Simulated DoLP and angle of linear polarization (AoLP) of the

optimized structure in (b) as a function of the wavelength for LCP and RCP light at normal

incidence. (d) Simulated reflection amplitudes r_{xx} and r_{yy}, and the relative phase difference $\Delta\varphi$

of the MIM structure with normally incident x- and y-polarized light, respectively.

In order to realize a broadband QWP, we implement three-dimensional full-wave simulations

with the commercially available software COMSOL Multiphysics (ver. 5.3) to optimize the

nanobrick dimensions (i.e., L_x and L_y), whereas the other geometrical parameters are kept

constant. In the simulation, the corners of the nanobrick are rounded with a radius of 5 nm to

avoid singularities and minimize the deviation between theory and experiments. Here the SiO$_2$ dielectric layer is regarded as a lossless material with a measured refractive index of ~1.57 (Figure S1 in Supporting Information), while the permittivity of Au is described by interpolated experimental values.[57] Periodic boundary conditions are applied in both the *x*- and *y*-directions of the unit cell, and a perfectly matching layer (PML) is used above the Au nanobrick to truncate the simulation domain. To excite the MIM unit cell, CP light is impinging normally on the structure from the top. Figure 1b shows the simulated degree of linear polarization (DoLP) as a function of the nanobrick dimensions (L_x and L_y) at the design wavelength of $\lambda = 850$ nm, defined by the Stokes parameters $\text{DoLP} = \sqrt{s_1^2 + s_2^2}/s_0$, which can fully describe the figure of merit of the QWP. From Figure 1b, it is clearly seen that the DoLP changes with the detuned nanobrick lengths and perfect circular-to-linear polarization conversion can be achieved with optimized dimensions. Besides excellent circular-to-linear polarization conversion at the design wavelength, the designed QWP maintains good performance over a broad wavelength range from 750 to 980 nm indicated by green dashed lines, where the DoLP is above 95%, corresponding to an operation bandwidth of 230 nm (Figure 1c). Additionally, the calculated angle of linear polarization (AoLP), defined as $\text{AoLP} = \frac{1}{2}\tan^{-1}\frac{s_2}{s_1}$, is virtually constant at the angles of ±45° for the RCP and LCP light respectively within the working wavelength range of 750–980 nm as shown in Figure 1c. If the topmost nanobrick is rotated by an angle of θ with respect to the *x*-axis, the DoLP remains almost constant while AoLP is linearly changed, indicating the orientation-independent property of the designed QWP (Figure S2 in Supporting Information).

To understand the physical mechanism of the designed QWP, we calculate the corresponding reflection amplitudes and the relative phase difference under the illumination of *x*- and *y*-polarized light at normal incidence (Figure 1d). From Figure 1d, it is evident that the nanobricks support detuned resonances for normally incident *x*- and *y*-polarized light,[58,59]

5

corresponding to dips in the reflection spectra. When the incident light is y-polarized, the electric dipole will first be excited along the short axis of nanobricks (i.e., y-direction) at short wavelength of λ = 740 nm. Since the middle spacer is subwavelength, the excited electric dipole will induce a mirrored dipole approximately in antiphase, thereby inducing the GSP mode or magnetic dipole resonance with strong magnetic field enhancement in the spacer (**Figure 2**a).[39] Similarly, the GSP resonance at λ = 950 nm will be induced once the incident light is switched to x-polarization (Figure 2b). Due to these detuned GSP resonances, the relative phase difference $\Delta\varphi$ reaches $\sim$ 90° at λ = 850 nm. At the same time, the reflection amplitudes have nearly identical values, thereby resulting in perfect broadband circular-to-linear polarization conversion at the design wavelength. In addition, since the performance of a QWP is still acceptable when the ratio of LP components of the reflected light is within the range 0.8–1.2 and the absolute change of $\Delta\varphi$ is less than 10°,[60] such a design can function as a broadband QWP in the wavelength range of 750–980 nm, which is consistent with the resonant wavelengths of the two GSP modes along the short- and long-axis of nanobricks.
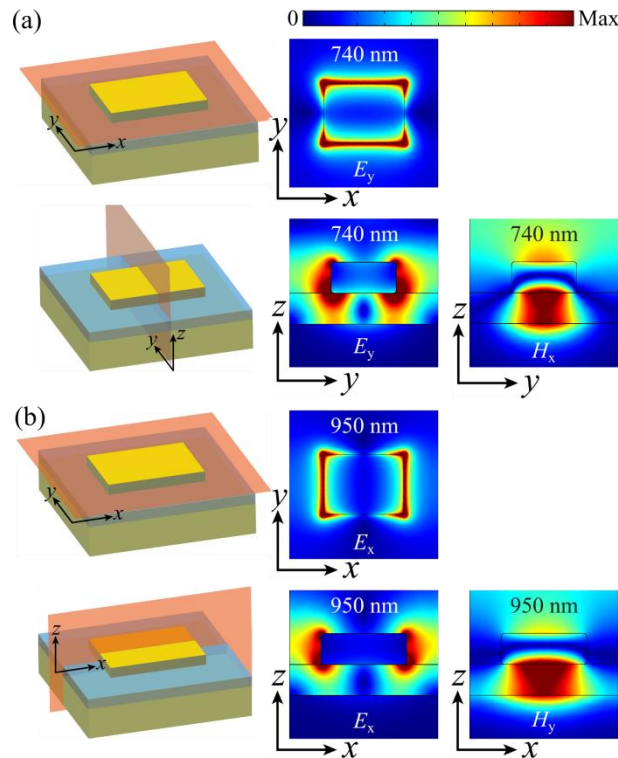
WILEY-VCH

Figure 2 (a) Normalized $|E_y|$ and $|H_x|$ distributions of the GSP resonance at $\lambda = 740$ nm when the incident light is LP along the y-direction. (b) Normalized $|E_x|$ and $|H_y|$ distributions of the GSP resonance at $\lambda = 950$ nm when the incident light is LP along the x-direction.

2.2. Experimental Demonstration of the Broadband QWP

In order to experimentally validate the broadband circular-to-linear polarization conversion, the proposed QWP was fabricated using electron-beam lithography (EBL) combined with thin-film deposition and lift-off process (see the Experimental section for more details of the fabrication). **Figure 3**a shows the scanning electron microscope (SEM) images of the fabricated sample, whose overall size is about 50×50 μm^2. Despite the surface roughness, the average dimensions of the fabricated nanobricks correspond well to the designed values. Following the fabrication, the fabricated sample is measured using a homemade optical setup shown in Figure 3b. The fiber-collimated near-infrared light from a tunable Ti: Sapphire laser (Spectra-Physics, Model 3900S) passes through a HWP (Thorlabs, AHWP05M-980), two linear polarizers (Thorlabs, LPVIS100-MP2), and a QWP (Thorlabs, AQWP05M-980) to generate a LCP or RCP beam with controlled intensity. Then the CP light is redirected and slightly focused on the sample with a spot size smaller than the sample area by using a beam splitter (Thorlabs, BS017) and a long working distance objective (Mitutoyo, 10x magnification, NA = 0.28). After that, the reflected signal transmitting through the same beam splitter is collected by a microscope imaging system that includes a long working distance objective (Mitutoyo, 50x magnification, NA = 0.55), a tube lens, a linear polarizer (i.e., analyzer) and a charge-coupled device (CCD) camera (Mightex).
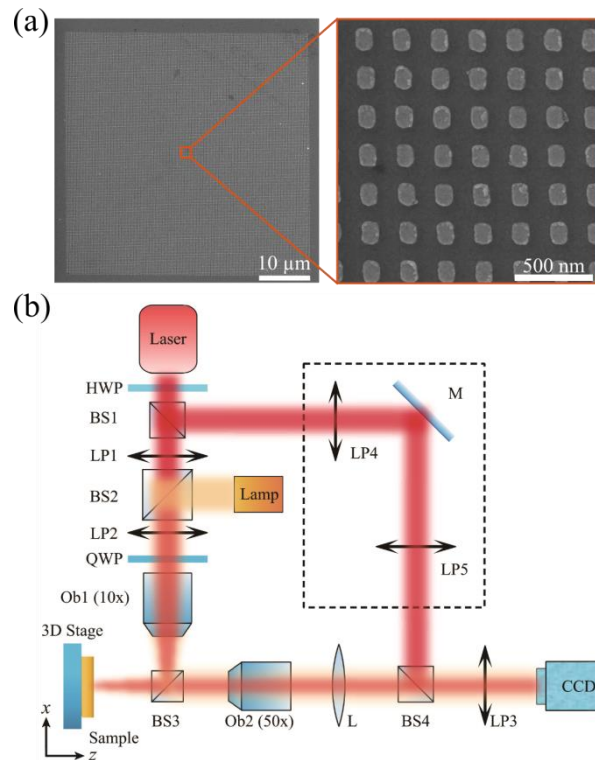
7

Figure 3 (a) SEM images of the fabricated QWP. (b) Schematic of the optical setup for characterizing the QWP. HWP: half-wave plate, BS: beam splitter, LP: linear polarizer, QWP: quarter-wave plate, Ob: objective, L: lens, M: mirror. The additional optical path marked within the dashed line is for interference experiment used in the VVB characterization.

To verify the performance of the fabricated sample, the intensity distributions with different orientations of a linear analyzer are recorded using the CCD camera. **Figure 4** displays the measured and simulated polarization states of the reflected beam at the wavelengths of $\lambda = 800$, 850 and 900 nm. It is observable that the measured states of polarizations well assemble the cosine-shaped patterns, confirming the high DoLP of the reflected light. In addition, the measured results are in reasonable agreement with the simulated ones except for the deviation of AoLP. For RCP incident light, the measured AoLP is between 55° and 60°, thus deviating from the predicted value of ~45°. This noticeable discrepancy may be ascribed to the imperfect performance of the optical components, especially the broadband QWP, as well as misalignment of the optical setup and rotation errors during measurement, thereby resulting in

8

non-ideal CP incident light.[31] As expected, the fabricated sample exhibits good performance at λ = 750 and 950 nm (Figure S3 in Supporting Information), validating the wide bandwidth. After integrating far-field intensities, we find that the measured reflectance is approximately ~85% on average, which is in good agreement with the simulated value of 88%. Therefore, the fabricated QWP sample enables efficient circular-to-linear polarization conversion in a wide wavelength spectrum ranging from 750 to 950 nm.
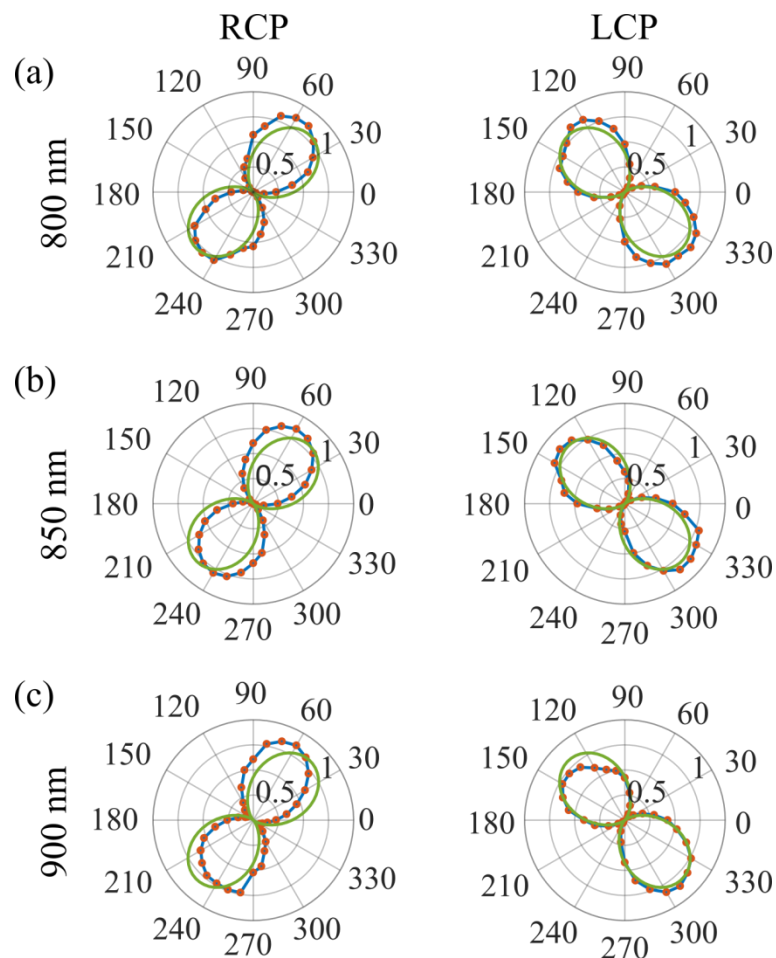

Figure 4 Simulated (green line) and measured (blue line with red dot) reflectance as a function of the orientation of a analyzer in front of the CCD camera for normally incident RCP and LCP light at wavelengths of (a) 800 nm, (b) 850 nm and (c) 900 nm. The measured results were averaged over three independent measurements and the relative error is within 5%.

2.3. QWP for Vector Vortex Beam (VVB) Generation

In addition to the aforementioned functionality of converting a CP incident wave to a LP wave with homogeneous polarization distribution in reflection, the designed QWP can tailor the polarization state locally and generate cylindrical vector-beams possessing spatially varied polarization vectors. To realize the VVB generator, we first consider the subwavelength unit cell shown in Figure 1a that functions as a local QWP with nearly equal amplitudes along the fast and slow axes, which can be described by the Jones matrix:

$$M = |r|e^{i\pi} \begin{bmatrix} sin(\theta)^2 - i \cdot cos(\theta)^2 & (-i-1)sin(\theta)cos(\theta) \\ (-i-1)sin(\theta)cos(\theta) & -i \cdot sin(\theta)^2 + cos(\theta)^2 \end{bmatrix} \quad (1)$$

where r is the reflection amplitude, π is the phase shift due to reflection, and θ is the orientation of the fast axis with respect to the x-axis. Considering a normally incident RCP beam $E_{in} = \frac{1}{\sqrt{2}}\begin{bmatrix} 1 \\ -i \end{bmatrix}$, the reflected beam will be LP, which can be written as:

$$E_{out} = ME_{in} = |r|e^{-i\left(\theta+\frac{\pi}{2}\right)} \begin{bmatrix} cos\left(\theta + \frac{\pi}{4}\right) \\ sin\left(\theta + \frac{\pi}{4}\right) \end{bmatrix} \quad (2)$$

If the $\theta + \pi/4$ equals the azimuthal angle φ with $\varphi = \tan^{-1}\left(\frac{y}{x}\right)$, then the reflected light $E_{out} = |r|e^{i\left(-\varphi-\frac{\pi}{4}\right)}\begin{pmatrix} cos\,\varphi \\ sin\,\varphi \end{pmatrix}$ will be locally polarized and AoLP is identical to φ. Therefore, a RP beam can be achieved by locally rotating the orientation of each nanobrick with an angle of $\theta = \tan^{-1}\left(\frac{y}{x}\right) - \frac{\pi}{4}$, as shown in **Figure 5**a. Meanwhile, additional spiral phase is introduced, thereby allowing for VVB generation that carries a specific OAM with the topological charge of $l = -1$. Once the incident light is switched to LCP with $E_{in} = \frac{1}{\sqrt{2}}\begin{bmatrix} 1 \\ i \end{bmatrix}$, we can get the similar output:

$$E_{out} = |r|e^{i\left(\varphi-\frac{3\pi}{4}\right)} \begin{bmatrix} cos\left(\varphi - \frac{\pi}{2}\right) \\ sin\left(\varphi - \frac{\pi}{2}\right) \end{bmatrix} \quad (3)$$

which represents an AP beam carrying OAM of $l = +1$. As such, by spatially rotating the nanobricks around their corresponding centers, the incident CP light can be transformed into a VVB. Additionally, the sign of the topological charge will be reversed once the incident spin is altered.
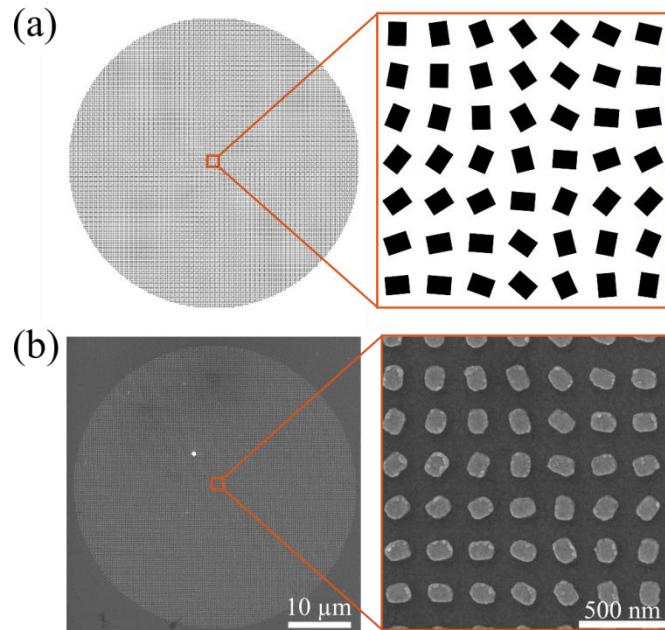

Figure 5 (a) Geometry of the metasurface-based VVB generator. (b) SEM images of the fabricated VVB generator.

Figure 5b presents the SEM images of the fabricated VVB generator with a diameter of 50 μm, which is composed of identical MIM elements with spatial-variant orientations. Following the fabrication, the reflected intensity distributions at different wavelengths were measured using the same setup shown in Figure 3b. By rotating the polarization analyzer in front of the CCD camera, the polarization states of the output beams are sketched in the left columns as shown in **Figure 6**. Under RCP illumination, typical anti-"s"-shaped patterns are experimentally formed after the output beam passes through an analyzer with different orientations, indicating the generation of a RP beam at the design wavelength of $\lambda = 850$ nm (first row in Figure 6b). Such anti-"s"-shaped pattern is related to the helicity phase profile

with the topological charge of $l = -1$ and further confirmed by the interference pattern of the reflected beam and a co-propagating Gaussian beam with a tilted angle. To conduct the interference experiment, a reference Gaussian beam passes through a few optical components shown in the dashed box in Figure 3b, and is finally added to interfere with the generated VVB. In the interference pattern, one can observe the fork dislocation marked with the dashed lines, verifying the phase singularity. Once the incident light is switched to LCP, an AP vortex beam is generated and the intensity distributions changes to an "s"-shape, resulting from the reversed topological charge of $l = +1$ (second row in Figure 6b), opposite to the case of RCP excitation. Importantly, it is also found that the measured far-field intensity distributions show a good resemblance between different wavelengths, unambiguously validating the broadband nature of VVB generation (Figure 6a, 6c, and Figure S4 in Supporting Information).
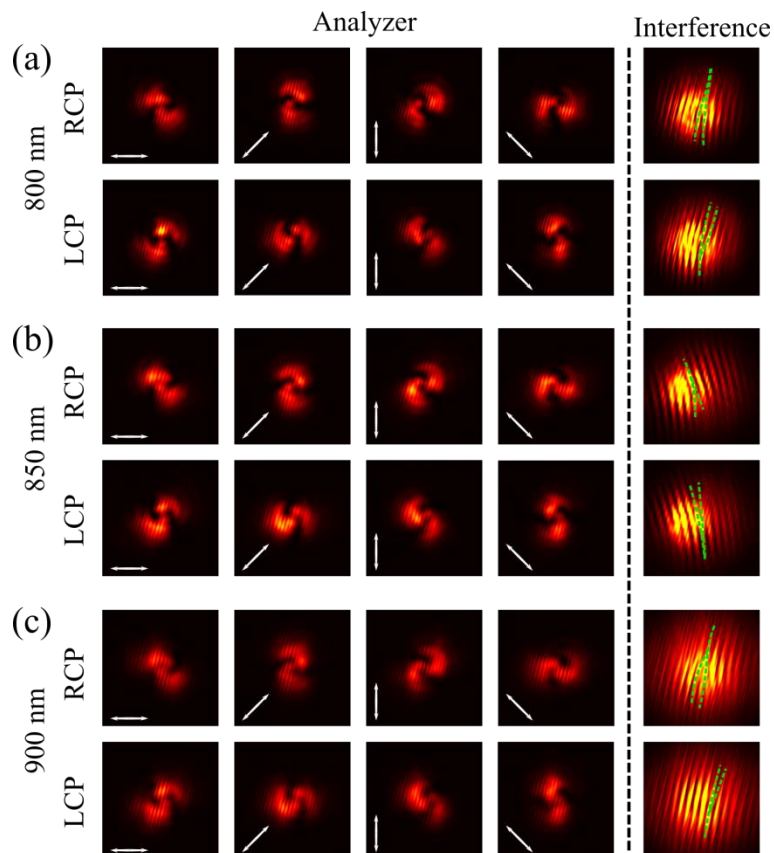

Figure 6 Measured far-field intensity distributions of the VVB generator for normally incident RCP and LCP light at wavelengths of (a) 800 nm, (b) 850 nm and (c) 900 nm. The

intensity distributions are measured with a polarization analyzer in front of the CCD camera. The right column shows the interference pattern of the generated VVB and a co-propagating Gaussian beam when the beam axes are tilted with respect to each other. The white double-headed arrows show the direction of the transmission axis of the linear polarization analyzer.

To further analyze the working performance of the designed VVB generator, the corresponding absolute efficiency, which is defined as the ratio of the power in the generated VVB over the total incident power, is calculated and given in **Figure 7**. As depicted in Figure 7, the measured efficiencies are sufficiently high over a wavelength range from 750 to 950 nm, with the averaging values of ~72% and ~68% for the RCP and LCP incident light, respectively, which is consistent with the aforementioned efficient QWP. In particular, we measured ~78% and ~66% converted efficiencies for RP and AP vortex beams under the RCP and LCP excitation at the design wavelength of $\lambda = 850$ nm, respectively. We believe that the slight difference in the efficiencies for RCP and LCP excitations is mainly related to the imperfect performance of optical components, particularly the QWP and the beam splitter, together with inevitable alignment and rotation errors, which affect the polarization state of incident CP light. Thus, the incident light becomes elliptically polarized rather than circularly polarized, resulting in different efficiencies.
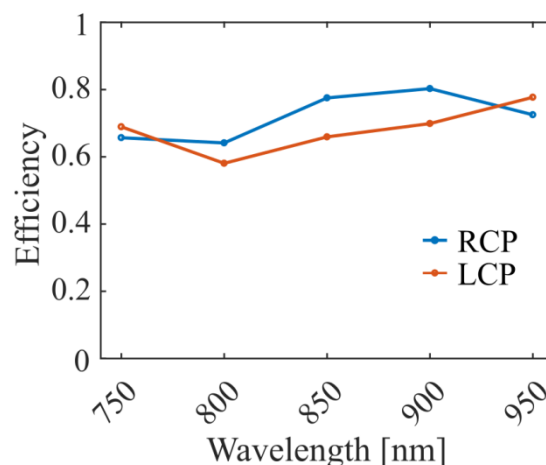
Figure 7 Measured efficiency of the VVB as a function of wavelength for RCP and LCP incident light, respectively. The efficiencies were averaged over three independent measurements and the relative error is within 5%.

3. Conclusion

In this work, we have experimentally demonstrated an ultrathin QWP based on the GSP metasurface, which allows for broadband circular-to-linear polarization conversion with ~85% average reflectance across a 200-nm-wide bandwidth in the near-infrared range (750–950 nm). Capitalizing on the QWP design, we have proposed a general method to generate VVBs by using spatially oriented QWP unit cells. The fabricated metasurface enables efficient generation of RP and AP beams that possess spatially-varied distribution of the polarization vector while carrying OAMs of $l = -1$ and $l = +1$, over a wavelength range from 750 to 950 nm, with the averaging efficiencies of ~72% and ~68% for the RCP and LCP incident light, respectively. This approach allows one to create planar, compact, and high-performance polarization converters to generate various structured beams, offering thereby new fascinating possibilities for quantum optics.

4. Experimental Section

Fabrication: All the samples were fabricated with standard EBL process combined with thin-film deposition. First, the 100-nm-thick Au and 50-nm-thick SiO_2 layers were grown on a double-polished silicon (Si) wafer by electron-beam evaporation and radio frequency (RF) magnetron sputtering, respectively. In order to make the thin-films adhesive to each other, 3 nm titanium (Ti) adhesion layers were added between the Si-Au and Au- SiO_2 interfaces via electron-beam evaporation. After that, a 100-nm-thick PMMA (2% in anisole, Micro Chem) layer was spin-coated on the prepared substrate, baked at 180°C, and exposed with a 30 keV

electron-beam. After exposure, the designed pattern was developed in the solution composed of methyl isobutyl ketone (MIBK): isopropyl alcohol (IPA) = 1: 3 for 30 s followed by 30 s in an IPA bath. A 3 nm Ti adhesion layer and the 50 nm top Au layer were successively deposited using thermal evaporation. Finally, the sample was placed in an acetone bath for more than 12 h, and the excess gold was removed using ultra-sonication for 15 s. The average dimensions of the nanobricks after lift-off correspond to the designed values of $L_x = 138$ nm and $L_y = 105$ nm.

Supporting Information
Supporting Information is available from the Wiley Online Library or from the author.

References

[1]   F. L. Pedrotti, L. S. Pedrotti, *Introduction to Optics*, Prentice Hall, **1993**.

[2]   N. Yu, F. Capasso, *Nat. Mater.* **2014**, *13*, 139.

[3]   P. Genevet, F. Capasso, F. Aieta, M. Khorasaninejad, R. Devlin, *Optica* **2017**, *4*, 139.

[4]   F. Ding, A. Pors, S. I. Bozhevolnyi, *Rep. Prog. Phys.* **2018**, *81*, 026401.

[5]   N. Yu, P. Genevet, M. A. Kats, F. Aieta, J. P. Tetienne, F. Capasso, Z. Gaburro, *Science* **2011**, *334*, 333.

[6]   X. Ni, N. K. Emani, A. V. Kildishev, A. Boltasseva, V. M. Shalaev, *Science* **2012**, *335*, 427.

[7]   S. Sun, K. Y. Yang, C. M. Wang, T. K. Juan, W. T. Chen, C. Y. Liao, Q. He, S. Xiao, W. T. Kung, G. Y. Guo, L. Zhou, D. P. Tsai, *Nano Lett.* **2012**, *12*, 6223.

[8]   A. Pors, O. Albrektsen, I. P. Radko, S. I. Bozhevolnyi, *Sci. Rep.* **2013**, *3*, 2155.

[9]   A. Pors, F. Ding, Y. Chen, I.P. Radko, S. I. Bozhevolnyi, *Sci. Rep.* **2016**, *6*, 28448.

[10]   F. Ding, S. M. Zhong, S. I. Bozhevolnyi, *Adv. Opt. Mater.* **2018**, *6*, 1701204.

[11]   F. Aieta, P. Genevet, M. A. Kats, N. Yu, R. Blanchard, Z. Gaburro, F. Capasso, *Nano Lett.* **2012**, *12*, 4932.

[12]   X. Ni, S. Ishii, A. V. Kildishev, V. M. Shalaev, *Light Sci. Appl.* **2013**, *2*, e72.

[13]   A. Pors, M. G. Nielsen, R. L. Eriksen, S. I. Bozhevolnyi, *Nano Lett.* **2013**, *13*, 829.

[14]   A. Arbabi, Y. Horie, M. Bagheri, A. Faraon, *Nat. Nanotechnol.* **2015**, *10*, 937.

[15]   M. Khorasaninejad, W. T. Chen, R. C. Devlin, J. Oh, A. Y. Zhu, F. Capasso, *Science* **2016**, *352*, 1190.

[16]   S. Wang, P. C. Wu, V. C. Su, Y. C. Lai, C. H. Chu, J. W. Chen, S. H. Lu, J. Chen, B. Xu, C. H. Kuan, T. Li, S. Zhu, D. P. Tsai, *Nat. Commun.* **2017**, *8*, 187.

[17]   M. S. Carstensen, X. Zhu, O. E. Iyore, N. A. Mortensen, U. Levy, A. Kristensen, *ACS Photonics* **2018**, *5*, 1665.

[18]   X. Ni, A. V. Kildishev, V. M. Shalaev, *Nat. Commun.* **2013**, *4*, 2807.

[19]   W. T. Chen, K. Y. Yang, C. M. Wang, Y. W. Huang, G. Sun, I. D. Chiang, C. Y. Liao, W. L. Hsu, H. T. Lin, S. Sun, L. Zhou, A. Q. Liu, D. P. Tsai, *Nano Lett.* **2014**, *14*, 225.

[20]   L. Huang, X. Chen, H. Mühlenbernd, H. Zhang, S. Chen, B. Bai, Q. Tan, G. Jin, K. W. Cheah, C. W. Qiu, J. Li, T. Zentgraf, S. Zhang, *Nat. Commun.* **2013**, *4*, 2808.

[21]   G. Zheng, H. Mühlenbernd, M. Kenney, G. Li, T. Zentgraf, S. Zhang, *Nat. Nanotechnol.* **2015**, *10*, 308.

[22]   P. Genevet, F. Capasso, *Rep. Prog. Phys.* **2015**, *78*, 024401.

[23]   S. Sun, Q. He, S. Xiao, Q. Xu, X. Li, L. Zhou, *Nat. Mater.* **2012**, *11*, 426.

[24]   J. Lin, J. P. B. Mueller, Q. Wang, G. Yuan, N. Antoniou, X. C. Yuan, F. Capasso, *Science* **2013**, *340*, 331.

[25]   L. Huang, X. Chen, B. Bai, Q. Tan, G. Jin, T. Zentgraf, S. Zhang, *Light Sci. Appl.* **2013**, *2*, e70.

[26]   A. Pors, M. G. Nielsen, T. Bernardin, J. C. Weeber, S. I. Bozhevolnyi, *Light Sci. Appl.* **2014**, *3*, e197.

[27]   F. Ding, R. A. Deshpande, S. I. Bozhevolnyi, *Light Sci. Appl.* **2018**, *7*, 17178.

[28]   A. Pors, M. G. Nielsen, S. I. Bozhevolnyi, *Optica* **2015**, *2*, 716.

[29]   J. P. B. Mueller, K. Leoson, F. Capasso, *Optica* **2016**, *3*, 42.

[30]   E. Maguid, I. Yulevich, D. Veksler, V. Kleiner, M. L. Brongersma, E. Hasman, *Science* **2016**, *352*, 1202.

[31]   F. Ding, A. Pors, Y. Chen, V. A. Zenin, S. I. Bozhevolnyi, *ACS Photonics* **2017**, *4*, 943.

[32]   A. Pors, M. G. Nielsen, S. I. Bozhevolnyi, *Opt. Lett.* **2013**, *38*, 513.

[33]   A. Pors, S. I. Bozhevolnyi, *Opt. Express* **2013**, *21*, 2942.

[34]   Y. Yang, W. Wang, P. Moitra, I. I. Kravchenko, D. P. Briggs, J. Valentine, *Nano Lett.* **2014**, *14*, 1394.

[35]   F. Ding, Z. Wang, S. He, V. M. Shalaev, A. V. Kildishev, *ACS Nano* **2015**, *9*, 4111.

[36]   S. C. Jiang, X. Xiong, Y. S. Hu, Y. H. Hu, G. B. Ma, R. W. Peng, C. Sun, M. Wang, *Phys. Rev. X* **2014**, *4,* 021026.

[37]   N. K. Grady, J. E. Heyes, D. R. Chowdhury, Y. Zeng, M. T. Reiten, A. K. Azad, A. J. Taylor, D. A. Dalvit, H. T. Chen, *Science* **2013**, *340*, 1304.

[38]   P. C. Wu, W.-Y. Tsai, W. T. Chen, Y.-W. Huang, T.-Y. Chen, J.-W. Chen, C. Y Liao, C. H. Chu, G. Sun, D. P. Tsai, *Nano Lett.* **2017**, *17*, 445.

[39]   F. Ding, Y. Yang, R. A. Deshpande, S. I. Bozhevolnyi, *Nanophotonics* **2018**, *7*, 1129.

[40]   Q. He, S. Sun, S. Xiao, L. Zhou, *Adv. Opt. Mater.* **2018**, *40*, 1800415.

[41]   F. Cardano, E. Karimi, S. Slussarenko, L. Marrucci, C. de Lisio, E. Santamato, *Appl. Opt.* **2012**, *51*, C1.

[42]   H. Chen, J. Hao, B. F. Zhang, J. Xu, J. Ding, H. T. Wang, *Opt. Lett.* **2011**, *36*, 3179.

[43]   Q. Zhan, *Adv. Opt. Photon.* **2009**, *1*, 1.

[44]   J. Ng, Z. Lin, C. T. Chan, *Phys. Rev. Lett.* **2010**, *104*, 103601.

[45]   A.M. Yao, M. J. Padgett, *Adv. Opt. Photon.* **2011**, *3*, 161.

[46]   J. Wang, J.-Y. Yang, I. M. Fazal, N. Ahmed, Y. Yan, H. Huang, Y. Ren, Y. Yue, S. Dolinar, M. Tur, A. E. Willner, *Nat. Photon.* **2012**, *6*, 488.

[47]   V. D'Ambrosio, E. Nagali, S. P. Walborn, L. Aolita, S. Slussarenko, L. Marrucci, F. Sciarrino, *Nat. Commun.* **2012**, *3*, 961.

[48]   F. Zhang, H. Yu, J. Fang, M. Zhang, S. Chen, J. Wang, A. He, J. Chen, *Opt. Express* **2016**, *24*, 6656.

[49]   J. Li, S. Chen, H. Yang, J. Li, P. Yu, H. Cheng, C. Gu, H.T. Chen, J. Tian, *Adv. Funct. Mater.* **2015**, *25*, 704.

[50]   P. Genevet, N. Yu, F. Aieta, J. Lin, M. A. Kats, R. Blanchard, M. O. Scully, Z. Gaburro, F. Capasso, *Appl. Phys. Lett.* **2012**, *100*, 013101.

[51]   E. Karimi, S. A. Schulz, I. De Leon, H. Qassim, J. Upham, R. W. Boyd, *Light Sci. Appl.* **2014**, *3*, e167.

[52]   M. Pu, X. Li, X. Ma, Y. Wang, Z. Zhao, C. Wang, C. Hu, P. Gao, C. Huang, H. Ren, X. Li, F. Qin, J. Yang, M. Gu, M. Hong, X. Luo, *Sci. Adv.* **2015**, *1*, e1500396.

[53]   S. Mei, M. Q. Mehmood, S. Hussain, K. Huang, X. Ling, S. Y. Siew, H. Liu, J. Teng, A. Danner, C.-W. Qiu, *Adv. Funct. Mater.* **2016**, *26*, 5255.

[54]   M. Q. Mehmood, S. Mei, S. Hussain, K. Huang, S. Y. Siew, L. Zhang, T. Zhang, X. Ling, H. Liu, J. Teng, A. Danner, S. Zhang, C.-W. Qiu, *Adv. Mater.* **2016**, *28*, 2533.

[55]   X. Yi, X. Ling, Z. Zhang, Y. Li, X. Zhou, Y. Liu, S. Chen, H. Luo, S. Wen, *Opt. Express* **2014**, *22*, 17207.

[56]   F. Yue, D. Wen, J. Xin, B. D. Gerardot, J. Li, X. Chen, *ACS Photonics* **2016**, *3*, 1558.

[57]   P. B. Johnson, R. W. Christy, *Phys. Rev. B* **1972**, *6*, 4370.

[58]   A. Pors, M. G. Nielsen, G. D. Valle, M. Willatzen, O. Albrektsen, S. I. Bozhevolnyi,

Opt. Lett. **2011**, *36*, 1626.

[59]   H. Zhao, Y. Yang, Q. Li, M. Qiu, *Appl. Phys. Lett.* **2013**, *103*, 261108.

[60]   Y. Zhao, A. Alù, *Phys. Rev. B* **2011**, *84*, 205428.

Broadband quarter-wave plates (QWPs) with ~85% average reflectance across a 200-nm-wide bandwidth have been demonstrated with gap-surface plasmon metasurfaces in the near-infrared range. Furthermore, vector vortex beams (VVBs) have be realized by using space-variant QWP unit cells and the fabricated metasurface exhibits highly-efficient VVB generation, with the average efficiencies of ~72% and ~68% for the right and left circularly-polarized incident waves, respectively.

Jacob T. Heiden, Fei Ding*, Jes Linnet, Yuanqing Yang, Jonas Beermann, and Sergey I. Bozhevolnyi

Gap-surface Plasmon Metasurfaces for Broadband Circular-to-linear Polarization Conversion and Vector Vortex Beam Generation

ToC figure

WILEY-VCH
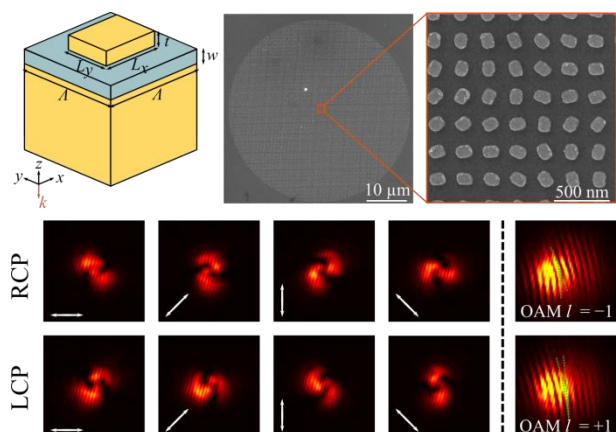
Supporting Information

Gap-surface Plasmon Metasurfaces for Broadband Circular-to-linear Polarization Conversion and Vector Vortex Beam Generation

Jacob T. Heiden, Fei Ding*, Jes Linnet, Yuanqing Yang*, Jonas Beermann, and Sergey I. Bozhevolnyi

Section S1. Refractive index of the deposited SiO₂ measured with Ellipsometer.

To measure the refractive index of SiO$_2$, we first deposited 50-nm-thick SiO$_2$ layer on a double-polished Si wafer by RF magnetron sputtering. Then we used the ellipsometer (SE200BM) to measure the refractive index by analyzing reflected light of different polarizations from the sample.
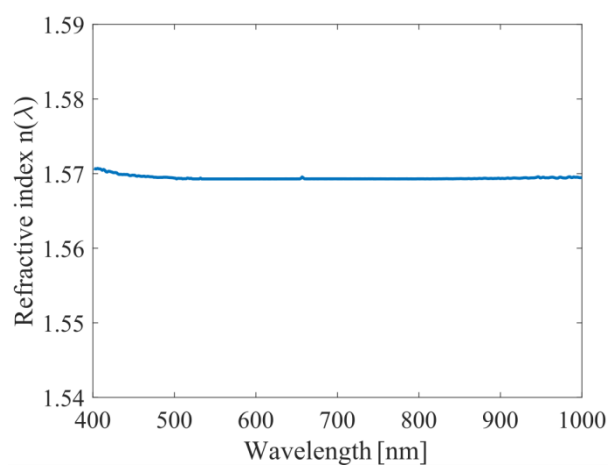

Figure S1. Measured refractive index of the deposited SiO$_2$ spacer layer.

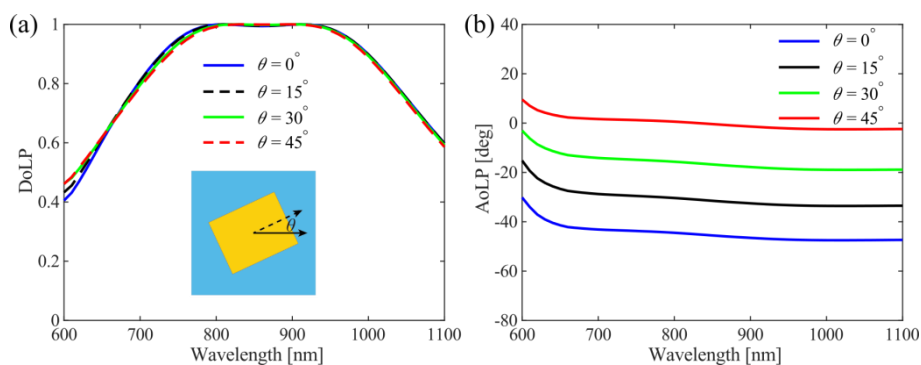**Section S2. Simulated orientation-independent property of the designed QWP**

Figure S2. Simulated orientation-independent property of the designed QWP. In the simulation, the topmost nanobrick is rotated by an angle of θ with respect to the x-axis.

Section S3. Simulated and measured reflectance as a function of the orientation of the analyzer at wavelengths of 750 and 950 nm.
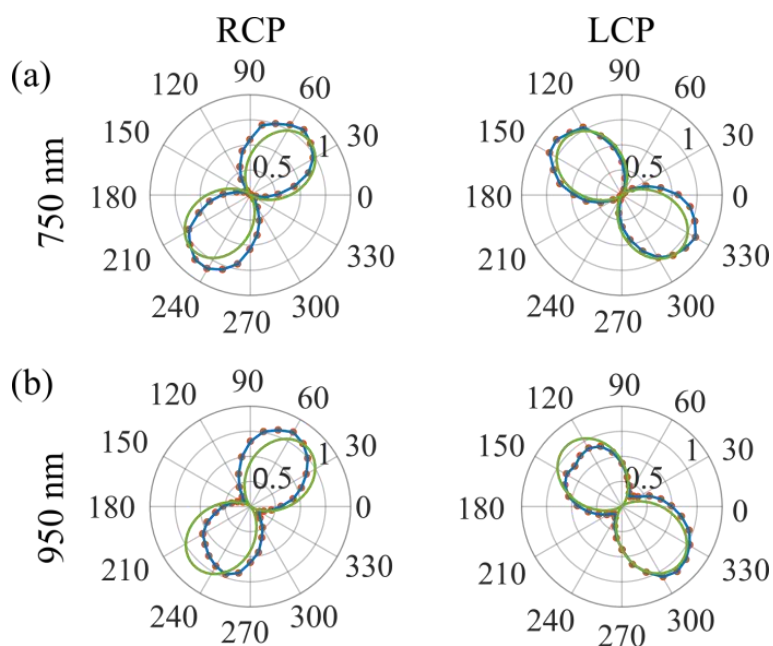

Figure S3. Simulated (green line) and measured (blue line with red dot) reflectance as a function of the orientation of the analyzer in front of the CCD camera for normally incident RCP and LCP light at wavelengths of (a) 750 nm and (b) 950 nm.

Section S4. Measured far-field intensity distributions of the VVB generator for normally incident RCP and LCP light at wavelengths of 750 nm and 950 nm.
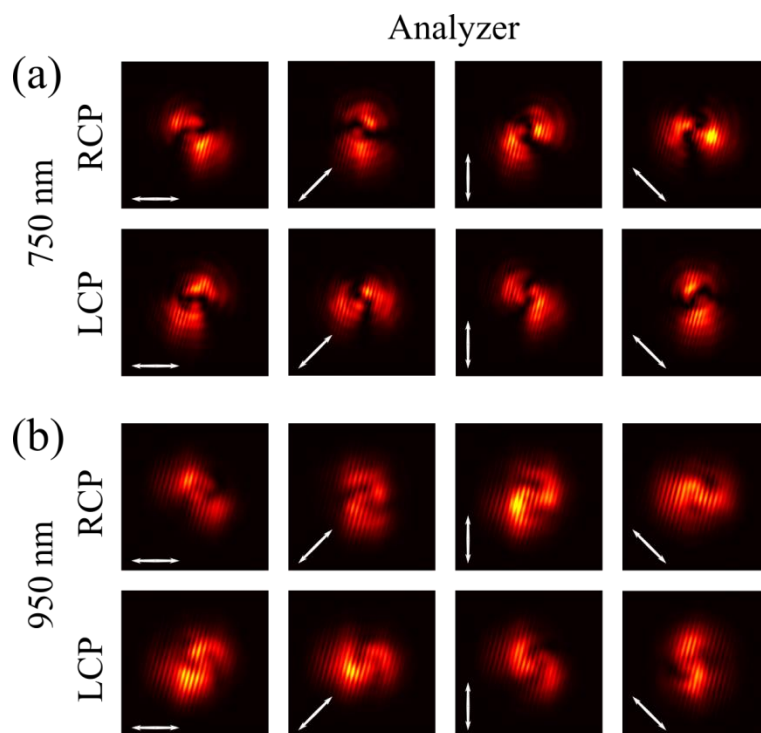

Figure S4. Measured far-field intensity distributions of the VVB generator for normally incident RCP and LCP light at wavelengths of (a) 750 nm and (b) 950 nm. The intensity distributions are measured with a polarization analyzer in front of the CCD camera. The white double-headed arrows show the direction of the transmission axis of the linear polarization.